TURBIDITE STACKING PATTERNS IN SALT-CONTROLLED MINBASINS: INSIGHTS FROM INTEGRATED ANALOGUE MODELS AND NUMERICAL FLUID FLOW SIMULATIONS

XIAOXI WANG[1], STEFAN M. LUTHI[1], DAVID M. HODGSON[2], DIMITRIOS SOKOUTIS[3], ERNST WILLINGSHOFER[3], REMCO M. GROENENBERG[4]

1. Department of Geoscience and Engineering, Delft University of Technology, Stevinweg 1, 2628 CN Delft, The Netherlands (E-mail: s.m.luthi@tudelft.nl)
2. School of Earth and Environment, University of Leeds, Leeds, LS2 9JT, The United Kingdom
3. Department of Earth Sciences, Utrecht University, Budapestlaan 4, 3584 CD Utrecht, The Netherlands
4. Petrotechnical Data Systems, Lange Kleiweg 10, 2288 GK Rijswijk, The Netherlands

ABSTRACT

The seafloor bathymetry of intraslope minibasins on passive continental margins plays a significant role in controlling turbidity current pathways and the resulting sediment distribution. The internal sediment stacking patterns remain poorly constrained due to the diversity of slope and minibasin configurations and the complicated interplay between turbidity current behaviour and evolving seafloor bathymetry. In this study, we combine laboratory analogue modelling of intraslope minibasin formation with numerical flow simulations of multi-event turbidity currents. This approach permits an improved understanding of evolving flow-bathymetry-deposit interactions and the resulting internal stacking patterns of the infills of such minibasins. The bathymetry includes a shelf-to-slope channel and an first minibasin separated by a confining ridge from two lower minibasins. The turbidity currents in the upper minibasin follow a series of stages from short initial ponding, filling-and-spilling and an extended transition to long retrogradational ponding. Upon reaching the minibasin floor the currents undergo a hydraulic jump, which greatly reduces their sediment-carrying capacity, and much sediment is deposited in the initial zone of subcritical flow. In the fill-and-spill stage, flow stripping and grain size partitioning allow the finer sediment to be transported across the confining ridge to lower areas that contain other minibasins. Overall, the sequences retrograde upstream with continued sedimentation due to longitudinal compensation accompanied by lateral switching into local depressions. Eventually, the basin infill retrogrades into the channel where cyclic steps with wavelengths of 1-2 km develop as a function of a pulsating flow. The results are at variance with conventional schemes that emphasise sequential downstream minibasin filling through ponding, and

they have important implications for locating the best reservoir-quality sands in the subsurface. Comparison of these results with published field and experimental examples seems to support the main conclusions.

Keywords Tectonic analogue modelling, numerical flow modelling, turbidity currents, intraslope minibasins, lateral compensation, longitudinal compensation, cyclic steps.

INTRODUCTION

Passive continental margins display a great diversity of seafloor bathymetries on their submarine slopes. In diapirically controlled settings, these bathymetries are characterized by numerous ridges and/or mini-basins, for example offshore the Gulf of Mexico (e.g., Diegel et al., 1995; Rowan and Weimer, 1998; Prather, 2000; Lamb et al., 2006; Hudec et al., 2013), offshore West Africa (e.g., Duval et al., 1992; Liro and Coen, 1995; Marton et al., 2000; Hudec and Jackson, 2004; Brun and Fort, 2011), offshore Brazil (e.g., Demercian et al., 1993; Cobbold et al., 1995; Roberts et al., 2004; Mohriak et al., 2012; Guerra and Underhill, 2012) and in the North Sea (e.g., Coward and Stewart, 1995; Kockel, 1998, Harding and Husse, 2015). Complicated seafloor bathymetries play a significant role in controlling turbidity current behaviour, sediment dispersal patterns and internal architectures of turbidite systems (Kneller and McCaffrey, 1999; McCaffrey and Kneller, 2001; Hodgson and Haughton, 2004; Gee and Gawthorpe, 2006; Lamb et al., 2006; Albertão et al., 2011, 2015; Oluboyo et al., 2014).

Concepts such as the fill-and-spill models (Winker 1996; Prather et al., 1998), the flow-stripping model (Sinclair and Tomasso 2002), and the silled sub-basins model and connected-tortuous-corridor model (Smith, 2004) have been proposed to explain and predict the filling history of successive intraslope minibasins. These models were developed from specific basin margins that are influenced by mud- or salt-diapirism, and they are conceptual because the architecture of basin infill could not be validated with high-resolution three-dimensional data. This lack of detail makes them difficult to apply to turbidite reservoirs in such settings.

Well-exposed outcrops with 3D control or high-resolution 3D seismic data could fill these resolution gaps, yet only few case studies contain such high quality data (Gervais et al., 2006; Moody et al., 2012). Most outcrops are two-dimensional and thus offer only partial information on the internal sedimentary architecture (Shanmugam and Moiola, 1991; Shanmugam, 2000; Satur et al., 2000). 3D seismic data of sufficiently high resolution is sometimes available from the shallow subsurface but is often of lesser interest as it contains rarely natural resources. The present study aims i) to integrate analogue models and numerical simulations to investigate flow-bathymetry-deposit interactions during the filling of salt withdrawal minibasins; ii) to investigate the evolution of sedimentary dispersal and stacking patterns at a bed-scale resolution; and iii) to discuss similarities and differences with existing conceptual models of minibasin infill.

METHODOLOGY

This study adopts a novel method that integrates laboratory analogue modelling of passive-margin seafloor bathymetries and numerical simulations of multiple turbidity currents.

In a first step, laboratory analogue tectonic experiments using “sandbox” models permitted realistic seafloor geomorphologies to be obtained that were digitized and upscaled. The bathymetry serves as input surface for the numerical flow modeling, for which the process-based FanBuilder software is used that simulates low-density turbidity currents (Groenenberg et al., 2009, 2010). A series of parameters within ranges expected to occur in nature constrained the flow simulations. Multiple flow events are run in a single experiment such that the bathymetry continuously evolvesd with each new flow. The resulting sedimentary sequences are then analyzed in 3-D in a series of strike and dip sections, and as 1D pseudo-logs.

ANALOGUE TECTONIC EXPERIMENTS

“Sandbox” analogue experiments are widely used to model the evolution of a large variety of deformation types in structural geology and tectonics (e.g., Colletta, et al., 1991; Sokoutis and Willingshofer, 2011; Willingshofer et al., 2013). Analogue models driven by gravitational forces have proven to be effective in helping to understand deformation mechanisms caused by salt tectonics on passive continental margins such as along the Gulf of Mexico and the South Atlantic margins (e.g., Vendeville and Cobbold, 1988; Cobbold and Szatmari, 1991; Vendeville and Jackson, 1992a, b; Brun and Fort, 2004, 2011). These margins are characterized by a transition from upslope extension to downslope compression caused by gravity sliding and spreading of the brittle-ductile package. In this study, the successful laboratory modeling of the Angolan passive margin conducted by Fort et al. (2004) and Brun and Fort (2004, 2011) has been taken for reference, and similar techniques and parameters are adopted here.

Silicone putty overlain by sand are used to represent the prekinematic salt and sediment respectively (Vendeville and Jackson, 1992a, b; Weijermars et al., 1993), while a plastic sheet placed under the silicone represents a weak décollement layer (McClay, 1990; Allemand and Brun, 1991). The silicone putty used is SGM-36 (Mark of Down Corning) with a density of about 965 kg/m^3 and a viscosity of 5×10^4 Pa·s; it is applied with a thickness of 8 mm. Weijermars (1986a, b, 1993) has demonstrated in a series of experiments the ability of this material to provide a rheologically-scaled analogue of salt. The overlying sand chosen here to represent the sedimentary sequence has a mean grain size of 0.3 mm, a density of about 1500 kg/m3 (uncompacted and in air) and a coefficient of friction of 0.9 without significant cohesion (Willingshofer et al., 2005); it is applied with a thickness of 10 mm. The model area is 50 cm wide and120 cm long, with the sand-silicone layers resting on two linked horizontal plates that divide the model into two parts of 80 cm (Plate 1) and 40 cm (Plate 2) (Fig. 1). The experiment is started by tilting Plate 1 to an angle of 4°. During the entire duration of the experiment, the layers are completely confined by metal bars on all sides. No sediment is added to the model in order to allow the formation of minibasins and ridges without them getting infilled with synkinematic sediments. A digital 3D laser installed above the model scans every 30 minutes the evolving topography, which simulates the seafloor bathymetry.. After 68 hours the tectonic structure was pronounced and judged to be realistic enough for the experiment to be stopped (Fig. 2A).

The cross-section of the result displays three distinctive structural domains: extension, translation and compression (Fig. 2B). In the upper part, well-developed extensional structures formed, such as normal faults, grabens, minibasins and diapirs between rafts (Fig. 2B). The maturity of the diapirs generally decreases downdip as a result of the extensional structures in the upper slope area occurring earlier than those further downdip. The transitional zone underwent a downward slab-like movement on the décollement sheet. In the compressional domain, folds and thrusts are dominant and restricted to the toe of the slope (Fig. 2B). The compressional domain migrates in both the downdip as well as the updip direction, as can be deduced from the prograding directions of the folds forming on both sides of the imbricated folds and thrusts.

THE INPUT BATHYMETRY

The scanned 3D data of the uppermost, extensional domain (250 mm in the downdip direction) of the final tectonic model forms the digital elevation model, which is upscaled by a factor of 8×10^4 with a cell size of 250 m. This increased the scale of the modelled minibasin to a few to tens of kilometres in diameter, which are dimensions of typical minibasins in nature (e.g., Hudec et al., 2009; Fort et al., 2004; Loncke et al., 2006). To obtain a more realistic continental margin configuration and to reduce the boundary effects, a shelf area with a width of 10 km and a gradient of slightly less than 0.7° is added upslope by Kriging interpolation. The model area (Fig. 3A) measures 15 km by 30 km and contains an artificially imposed channel on the outer part of the shelf feeding downstream into an upper minibasin with confining slopes on all sides, followed by a slope-parallel ridge and several smaller minibasins that are followed again by a ridge (Fig. 3B). The channel is slightly curved and has a U-shaped cross-section profile with an average thalweg slope of ≈ 1.25°. It is about 70 m deep, 3 km wide (with a 1.5 km wide thalweg) and 10 km long, and it connects to the upper minibasin, which is 10 km wide and 5 km long with an almost circular central area. At the downstream bounding edge of the upper minibasin there is a counterslope of ~ 1.20° and a spillover point on the ridge that is about 60 m higher than the lowest point of the minibasin. The lee-side slope of the ridge is steeper with an average of ~ 2.60°, leading directly to two smaller, poorly-confined minibasins of about 2.5 km in diameter that are adjacent to each other.

FLOW SIMULATIONS

“FanBuilder” is a three-dimensional process-based model that simulates turbidity current hydrodynamics and sedimentation on an arbitrary bathymetry over multiple successive flow events (Groenenberg, 2007; Groenenberg et al., 2009). FanBuilder possesses the following two important characteristics for this study: (1) it is designed to simulate low-density turbidity currents with Newtonian fluid behaviour and (2) geomorphic features and autogenic processes such as channelization, channel aggradation and avulsion, and lobe switching in the resulting deposits can be observed in real-time. The model is based on five depth-averaged mathematical equations proposed by Parker et al. (1986). These five equations ensure the maintenance of flow momentum in the streamwise and transverse directions as well as flow mass and sediment mass conservation during one flow event but cannot handle higher-density currents above the Boussinesq approximation, i.e. with concentrations above about 7% in volume. A combined convection-diffusion equation governs sediment transport in this model. The model supports sediment transport of multiple grain-size classes and sediment exchange through erosion and deposition. The input parameters for the model include the initial bathymetry of the receiving basin, the grain size distribution of the sediment, the magnitude-frequency distribution of the flows, and the initial volume concentration of the sediment in the flows. By adjusting these parameters, their impact on the long-term stratigraphic evolution of successive turbidity current deposits can be simulated and studied. The evolution of the flows, such as the flow velocities, thicknesses and densities, and the densimetric Froude number, can be monitored in real time. The resulting stratigraphy in the form of the thickness and the mean grain size distribution of the deposits is instantaneously visible after each flow.

To ensure that FanBuilder is sufficiently realistic in simulating turbidity currents and their deposits, Groenenberg (2007) conducted two sets of validation experiments based on data from laboratory experiments. These included turbidity currents above a constant and smooth ramp by Luthi (1981) and experiments of turbidity currents encountering various shapes of obstacles by Kneller and McCaffrey (1995). The qualitative and quantitative comparison with these laboratory experiments were deemed sufficiently good for FanBuilder to be applied to larger-scale simulations that include natural settings and volumetric sediment concentrations not exceeding 7% (Groenenberg, 2007; Groenenberg et al., 2009). The applications included the simulations of submarine lobes based on data from outcrops exposed in the Karoo Basin, South Africa (Groenenberg et al., 2010) as well as predictive models of the impact of relay ramps on turbidity current pathways with different inflow angles (Athmer et al., 2010). These successful applications of FanBuilder provided the incentive to use the software in the present study.

NUMERICAL SIMULATION RESULTS

The results reported here are from a set of 100 flow experiments whereby the inflow conditions were slightly supercritical as the densimetric Froude number lies just above 1, and in equilibrium as the resistance to flow is equal to the gravitational acceleration. The parameters to achieve these conditions include the flow velocity, the sediment concentration, the flow depth and the drag coefficient. Additional parameters defined include the initial flow width, the total released sediment volume and the grain size composition (Table 1). They are constrained within the range of magnitudes published from the few turbidity currents that have been measured in nature, which are exclusively from low concentration flows (Talling et al. 2015). Measurements in nature include turbidity currents on the Mid-Atlantic Ridge with a flow thickness of 30 m, a flow velocity of 1.5-40 m/s and a concentration of 0.03-0.12 (Van Andel and Komar, 1969); turbidity currents in the incised channel (without spillover lobes) of Bute Inlet with a flow thickness of 30-40 m, a slope of 1.5°, a flow velocity of 3.35 m/s, a flow concentration of 0.005-0.01 and a maximum grain size of 0.480 mm (Zeng et al., 1991); four turbidity currents measured by Xu et al. (2004) with a flow-body thickness of 50 m and a maximum head velocity of 5-12 m/s along the canyon (Zeng and Lowe, 1997; Mulder and Alexander, 2001).

One hundred point-sourced flow events with identical flow parameters (Table 1) were run with the evolution of the flow and depositional characteristics monitored in real-time. For each flow the flow height, the densimetric Froude number, the depositional thickness and the mean grain size is recorded over the model area. Additionally, the total deposit thickness and average grain size of the entire sedimentary package was recorded. This allows for a continuous monitoring of the interplay between the evolving bathymetries, the flow behaviour, and the depositional characteristics.

Flow evolution

The results of the hundred successive flow events show that four different stages of flow evolution can be distinguished. The flows are numbered 1 for the first one to 100 for the last one.

Initial ponding stage

Full ponding of event 1 in the upper minibasin without any spill-over is observed (Fig. 4, top). After about 3000s, the flow volume is completely released into the channel and starts to enter the upper minibasin with a maximum flow velocity of about 6 m/s. After reaching the minibasin centre, the flow expands and shortly thereafter a hydraulic jump occurs, i.e. rapidly transitions from supercritical to subcritical, which decreases its velocity and increases its height. The flow is not capable of breaching the counterslope ridge and dissipates its entire energy in the upper minibasin.

Fill-and-spill stage

Flows 2 to 31 partially spill over the downstream ridge confining the upper minibasin and flow down the leeside slope into the lowermini-basins, most probably because the deposit of flow event 1 had already reduced the depth of the minibasin enough to permit this. Flow event 25 (Fig. 4, middle) is used as an example here to illustrate the flow evolution. The flow expands in the upper minibasin with its flanks becoming subcritical. The central part, however, does not undergo a hydraulic jump and remains supercritical and, due to its high velocity, climbs up the counterslope and flows down into the lower minibasins where the energy of the flow completely dissipates.

Transitional stage

This stage encompasses flow events 32 to 40 and is characterized by irregular switching between spill-over and minibasin-confined flows. Spill-over only happens in flow events 34, 36, 37 and 40 while in the remaining flows confinement prevails. This stage is therefore transitional between the previous and the subsequent stages.

Retrogradational ponding stage

For the remaining flows, from events 41 to 100, the turbidity currents are not able to spill over and remain trapped in the upper minibasin because retrogradational deposition on its counterslope ridge has accumulated to a level that is higher than the original ridge. Additionally, increasing deposition in the channel decreases the flow energy through a loss of sediment, but also through repeated hydraulic jumps caused by an increasingly irregular bathymetry. Figure 4 (bottom) illustrates this for the case of event 45.

Flow-deposit interaction

The deposits from the succession of flow events lead to an evolving bathymetric template that influences subsequent flow behavior. This in turn influences the sediment dispersal patterns, and notably the sediment thicknesses and grain sizes, with significant differences between the ponding, fill-and-spill and trapping stages.

Deposit and mean grain size

The depositional thickness map of bed 1 (Fig. 5) indicates two sites of significant deposition. One is at the inflow where a levee-shaped deposit is formed with a maximum thickness of about 1.80 m. The other one is on the counterslope of the upper minibasin with a maximum thickness of about 1 m. Both locations also have the coarsest mean grain size (Fig. 5).

The beds formed during the fill-and-spill stage, illustrated by events 2, 20 and 30 in Figure 5, are distributed over three minibasins. The thickest sediment is located in the upper minibasin. Erosion occurs on the lee-side of the confining ridge (blue areas in Fig. 5). In the early phase of this stage (e.g. bed 2), merely finer grains are transported to the lower minibasins by the spillover flows. Afterwards, the flows carry increasingly coarser grains over the bounding ridges to the lower minibasins, accompanied by stronger erosion on the downstream slope of the ridge (beds 20 and 30 in Fig. 5). The coarsest and thickest deposits are on the channel margins forming fledgling levees, the counterslopes of the three minibasins, and on the leeside of the bounding ridge.

At the transitional stage, spill-over becomes less frequent and eventually ceases. Even if the flows spill over, their grain size decreases downstream (bed 40 in Fig. 5), partly because deposition in the channel is seen to increase, forming very long-wavelength bedforms that contain some coarse material.

At the trapping stage, no deposition takes place in the lower minibasins. The accommodation in the upper minibasin is constantly shrinking (bed 60, 80 in Fig. 5) and the depocentre is moving upstream due to the back-stepping of the counterslope. The coarsest deposits are found in depressions in the channel spaced 1-2 kilometres apart where the flows become subcritical, while some minor erosion can be found in between them where the flows become supercritical (beds 80 and 100 in Fig. 5).

The thickness distribution of the entire 100-bed succession (Fig. 6) illustrates that the lower minibasins only received sediment during the first 40 flow events, while after that deposition was limited to the upper minibasin and the channel. The maximum deposit thickness is, however, found directly above the initial depocentre of the upper minibasin and amounts to slightly more than 80 m.

Bathymetric changes

The bathymetric evolution is shown in three time slices corresponding to flow events 40, 70 and 100 (Fig. 7). During the fill-and-spill stage, depositional ridges are seen to develop around the counterslope of the upper minibasin (Fig. 7A). They are obliquely orientated relative to the overall flow direction, probably caused by the complex interaction of large-scale vortices in the minibasin and backward flow from the counterslope (see e.g. flow 45 in Fig. 4). At the trapping stage, more depositional ridges form and divide the increasingly limited accommodation space into several segments. Similarly, the bedforms in the channel become more pronounced (Fig. 7B, C).

This evolution can also be observed in the longitudinal direction. Figure 7D shows that two internal ridges migrate upslope, starting around flow event 40, and increase in amplitude until they outgrow the original counterslope ridge of the upper minibasin. These ridges and the lowest bathymetric point shift upstream by 2 to 3 kilometres and grow such that effectively there are two spill points. The counterslope gradient changes through time too (Fig. 7E). Initially, the gradient decreases during the first 40 events when spill-over still occurred, and later increases from event 41 to event 50 when trapping starts, and gradually decreases thereafter during the remainder of the trapping stage (Fig. 7E).

Depositional architecture

The thickness and mean grains size distributions form the basis to subdivide the stratigraphy resulting from the 100 flow events into seven bedding units. These are related to the flow stages as follos: the initial ponding stage contains one Unit, the fill-and-spill stage three, the transitional stage one, and the retrogradational ponding stage two. Figure 8 shows the model area subdivided into five depositional zones (Fig. 8A) and the proportional distribution of the seven bedding units for each of these zones (Fig. 8B). With the exception of Unit 1, it is seen that the Units 2 to 7 show a steady regression towards the upstream area, while the lower minibasins receive less sediment and eventually become starved. The Units are subdivided according to their grain size and thickness trends. Figure 9 summarizes the seven units in longitudinal and lateral cross-sections, with their respective depocentres, defined here as the loci of greatest thickness, indicated by dots in the three minibasins.

Unit 1, consists of only one bed, deposited 42% of the sediment in the minibasin, most of it on the counterslope, with the remainder in the channel area.

Units 2 to 4 formed during the fill-and-spill phase. Unit 2, consists of beds formed by events 2 to 11, has 20% of its deposit in the channel, 58% in the upper minibasin and 22% in the lower minibasin area. The centre of the upper minibasin contains thin and fine-grained beds with a coarsening- and thickening-upward trend while on the counterslope the beds are much thicker and coarser grained with a thinning-upward trend, In the two lower minibasins, this unit is thin-bedded and fine-grained with the depocentres off-centered due to run-up of the flows caused by the off-axial location of these minibasins. (Fig. 9).Unit 3 comprises beds 12 to bed 20 and its sediment volume distribution is similar to Unit 2 (Fig. 8). More coarse sediment is deposited in the upper minibasin, particularly in its centre, while the lower minibasins received finer grains with a continued asymmetric infill that exhibits longitudinal and lateral shifting. Unit 4 is the last sequence of the fill-and-spill stage and comprises beds 21 to 31. Here 60% of the sediment is deposited in the upper minibasin, while the lower minibasins received 17% with 23% in the channel. The continued retrogradation causes coarser grains and thicker beds to be deposited in the upper minibasin centre and finer grains in thinner beds on its counterslope. In the two lower minibasins, the fining- and thinning-upward trends continued concomitant with the upstream migration of the depocentre, and the lateral shift towards the minibasin centre. The depocentre of the upper minibasin longitudinally remained on the counterslope but retrograded, with a new ridge forming with a slight depression between it and the original ridge (Fig. 9). Laterally, the depocentre moves towards the basin centre.

Unit 5 is from the transitional stage and comprises beds from events 32 to 40. In the upper minibasin deposition on the counterslope practically ceased, with most sediment being deposited on the upstream side of the newly formed ridge and similar in character to Unit 4. The volume of sediment transported to the lower minibasins decreased considerably (Fig. 8) and becomes even finer with very thin beds.

Units 6 and 7 are from the retrogradational ponding stage. Unit 6 comprises beds from events 41 to 70. Because the flows were trapped in the upper minibasin, no sedimentation took place in the lower minibasins. Overall, deposition shifted towards the main channel and the inflow area (Fig. 8). Beds in the upper minibasin are finer-grained than in the underlying units, as much coarse material is trapped upstream. The depocentre moves upstream with a second ridge followed by a depression forming upstream, while laterally the depocentre moved further towards the basin centre (Fig. 9). Unit 7 is formed by beds from events 71 to 100. The main sedimentation moves further upstream with the depocentre now located in the lower channel area and deposition in the minibasin greatly decreased, with finer-grained and thinner beds than in the underlying units.

DISCUSSION

Filling history

Conceptual fill-spill-bypass models for successive mini-basins downslope have been invoked by numerous researchers (Winker, 1996; Weimer et al., 1998; Beaubouef and Friedman, 2000; Badalini et al., 2000; Sinclair and Tomasso 2002). In one commonly applied model, the highest minibasin is filled with sediments to spill point whereafter subsequent flows bypass sediments to the next, lower minibasin (Prather et al., 1998). By contrast, a flow-stripping model proposed by Badalini et al. (2000) suggests that sequential minibasins could fill coevally. Sinclair and Tomasso (2002) described the four phases comprising this model as flow ponding, flow stripping, flow bypass and blanketing, basing their findings on flume experiments and outcrop studies. The results of the present study suggest that other filling modes are possible too. After an initial and very short-lived ponding phase, essentially two major phases are observed, the first one with partial spillover, and the second one with complete trapping in the highest minibasin. A transitional phase separated these two phases during which both flow modes occur. Thus, unlike previously reported models, the lower minibasins receive sediment in the initial phase of sedimentation and are thereafter cut-off from further sediment supply. The reason for this is the nature of the infill in the upper minibasin. Most sediment accumulates on the counterslope and from there retrogrades upstream while increasing the height of the ridge that separates it from the lower minibasins. Sedimentation on the counterslope occurs for two related reasons. Firstly, inertia carries the flows across the minibasin floor up the slope where they slow down and thus loose some of their sediment. Secondly, hydraulic jumps occur on the lower counterslope that increase the flow height but decrease the velocity and thus the transport capacity of the flows. The geometry of these hydraulic jumps, however, is complex as seen from the maps in Figure 4, with areas of super- and subcritical flow often occurring side-by-side. This is one of the main reasons for the laterally and longitudinally uneven basin infill pattern, as best demonstrated by the obliquely orientated ridges forming in the basin. It is the growth of these ridges with the associated retrogradational backstepping that leads to the reduction, and eventual cessation, of sediment supply from the lower minibasins.

Starting somewhere in the transitional phase, and perhaps initiated by the ridges, more hydraulic jumps occur in the upstream direction and eventually the entire channel is filled with bedforms and associated oscillations between super- and subcritical flow modes. These upstream migrating bedforms are interpreted as cyclic steps (Kostic and Parker, 2006; Kostic, 2011), and have typical wavelengths of 1-2 km. Similar low-amplitude long-wavelength features have been reported from the Monterey East channel by Fildani et al. (2006), from the Squamish prodelts (Hughes Clarke et al., 2012), from the San Mateo Canyon channel system by Covault et al. (2014) and from Zhong et al. (2015) in the South Taiwan Shoal canyon. In most of these cases the wavelengths of the cyclic steps are even longer than the ones found here, but that is also the case for the overall scale of these channel systems. At the trapping stage, and particularly in its late phase (Unit 7), these cyclic steps cause much of the coarser sediment to be deposited in the channel, depriving the upper minibasin of high capacity flows and thus leading to increasingly thinner and finer-grained deposits there. Thus while during the spill-and-fill and transitional stages much coarse sediment reaches the three minibasins, in the trapping stage there is a continuous shift of the coarser-grained deposits upstream and into the channel and inflow area.

During the latest infill phase with strongly reduced accommodation, the asymmetric infill and lateral shifting of the depocentre caused by the hydraulic jumps leads to the formation of a depositional slightly leveed channel on the left flank of the upper minibasin (Fig. 9B). Had the experiments continued to a complete fill of the upper minibasin, this channel would have likely been the preferred pathway for sediment bypass into the lower minibasins in a similar fashion as reported by Brunt et al. (2004) and Aas et al. (2010, 2014).

The important role of hydraulic jumps in the infill history of the minibasins could be argued to be a function of the boundary conditions of the model runs, and specifically of the supercritical inflow condition. Models performed with the same software and subcritical inflow conditions, however, indicate that the flows become supercritical after a short distance (Wang, 2015) and that the depositional history resembles the one described here.

Internal architecture and stacking pattern

Much of the infill of the upper minibasin shows a thickening-then-thinning upward in parallel with a coarsening-then-fining succession. While this pattern could be interpreted to be the result of progradation-aggradation-retrogradation (Hodgson et al. ,2006), the succession observed is the result of the retrogradation of the entire depositional system. The lower succession comprises finer-grained and thinner beds deposited at the upstream tail end of the initial deposits. The central succession comprises coarser-grained and thicker beds deposited in the central part of the retrograding system, while the uppermost succession consists of finer-grained and thinner beds depositeds at the downstream end of flows. The entire flow-axial movement of the depositional system is described as longitudinal compensation, while the cross-sections perpendicular to flow suggest some degree of lateral compensation (Fig. 9). Athough there are multiple internal shifts between beds and units of beds, the maximum deposit thickness in the upper minibasin lies exactly at the location of the lowest point in the original bathymetry (Fig. 6, right). The lower minibasins show a thinning- and fining-upward trend caused by the reduction of sediment supply as sediment if increasingly sequestered in the upper minibasin. Eventually, when the upper minibasin is completely filled and flow bypass occurs, these sequences would be overlain by coarser-grained deposits.

Analogies with natural settings

To validate the results obtained here sub-seismic observations from natural settings of confined turbidite systems, either from outcrops or in the subsurface, would be required. The large-scale lateral and longitudinal depositional shifts reported here would require excellent continuous outcrops over large distances. Nevertheless, there are some published data that the results reported here can be compared to. Moody et al. (2012) examined the outcrops of the Morillo Formation of the Ainsa Basin (Spain) for spatial and stratigraphic variations in geometry and dimensions of the channel elements in weakly confined channel systems. They found that the axial downdip area has the highest net sand content, which is similar to the results reported here where the coarser and thicker deposits in the upper minibasin are also mainly in the axial-downdip area. Amy et al. (2007, their figure 15) found a landward shift in the proximal depositional facies of a sub-basin of the Alpine foreland in the Grès de Peira Cava (SE France). A similar landward stacking pattern was obtained by process-based simulation of turbidity currents over the recreated seafloor bathymetry of the Peira Cava turbidite system (Aas et al., 2010, 2014). They offered two reasons that might contribute to this back-stepping pattern: (1) a net decline in sediment supply as a result of allogenic processes, and/or (2) a landward migration of the slope break. Their first hypothesis compares well with the insights gained here in that the sediment transported into the upper minibasin decreases due to an autogenic increase in deposition in the feeding channel. The second hypothesis was supported by evidence of an upward decrease of the slope-related facies. Finally, in an outcrop study of an exhumed intraslope lobe complex, Spychala et al. (2015) documented a landward shift in successive lobes related to the response to healing of transient accommodation above a partially filled slide scar.

Except for shallow high-frequency data, the reflection seismic method usually lacks the resolution to reveal the sedimentary details and small-scale stacking patterns needed to validate the results reported here. A typical seismic section of a salt-withdrawal minibasin shows an overall aggradational sequence in the minibasin centre (e.g., Winker, 1996), although depocentres are known to migrate as salt welds start to develop. Moreover, surface and subsurface layers often experience post-depositional processes such as compaction and tectonic deformation that change their original geometry and architecture and thus make it even more difficult to unravel internal details. Using high-resolution seismic data, Gervais et al. (2006) recognized retrograding units on the depositional relief of the previous deposits in a distal lobe of the confined Golo turbidite system (latest Pleistocene, offshore Corsica). The suggested hydrodynamic reasons for this retrogradational pattern are similar to the ones offered here. Flows are erosive in the depression before an obstacle, but spread and deposit their sedimentary loads on its slope.

Progressively, therefore, deposition creates new frontal mounds that causes further upstream stacking. Prather et al. (2012) documented the stratigraphic evolution of linked intraslope basins in the Brazos-Trinity depositional systems (western Gulf of Mexico) based on coring results and 3D seismic data. They focused on distinguishing the different aprons (low-relief ponded, high-relief ponded and perched aprons) in these minibasins. By carefully recognizing and tracing the depocentres of series 20-70 in basins II and IV, a general trend of upstream migration can be obtained (Fig. 10), which to some extent supports the upstream-stacking patterns in the modeling results presented here (Fig. 9).

CONCLUSIONS

A continental slope bathymetry with a feeder channel and minibasins separated by slope parallel ridges obtained from laboratory “sandbox” modeling was used to study the flow evolution and depositional infill by turbidity currents using a numerical process-based method. An important result is that the flows initially partly spill over the confining ridge of the uppermost minibasin, but that continued deposition modifies the bathymetry such that sediment supply to the lower minibasins is shut off and the upper minibasin gets filled retrogradationally, with the depocentres backstepping from the counterslope toward the channel.. A complex distribution of the hydraulic jumps in the upper minibasin is responsible for the development of complex internal ridges that move upstream and are responsible for trapping coarser-grained material, resulting in a fining-upward trend in the minibasin infill. These ridges probably induce supercritical to subcritical oscillations in the flows that eventually lead to the development of cyclic steps along the entire channel length. The depositional retrogradation eventually fills the uppermost minibasin almost to spill, with increasing amounts of sediment being deposited in the channel, resulting in coarsening-upward sequences. There is some supporting evidence from outcrop and seismic data that the processes and depositional patterns identified here are described in natural systems where resolution allows.

ACKNOWLEDGEMENTS

Xiaoxi Wang is supported by the Chinese Scholarship Council and the Netherlands top research school ISES (Integrated Solid Earth Systems). We thank Remco Groenenberg for assistance with the FanBuilder flow modeling software.

REFERENCES

Aas, T.E., Howell, J.A. Janocko, M., and **Jackson, C.A.-L.** (2010) Control of Aptian palaeobathymetry on turbidite distribution in the Buchan Graben, Outer Moray Firth, Central North Sea. Mar. and Petr. Geol. **27**, 412–434.

Aas, T.E., Basani, R., Howell, J. and **Hansen, E.** (2014) Forward modelling as a method for predicting the distribution of deep-marine sands: an example from the Peira Cava Sub-Basin. In: Sediment-Body Geometry and Heterogeneity: Analogue Studies for Modelling the Subsurface (Eds. A.W. Martinius, J.A. Howell and T.R. Good), Geol. Soc. Spec. Publ. 387, 247–269.

Albertão, G.A., Mulder, T. and **Eschard, R.** (2011) Impact of salt-related palaeotopography on the distribution of turbidite reservoirs: Evidence from well-seismic analysis and structural restorations in Brazilian offshore. Mar. and Petr. Geol. **28**, 1023–1044.

Albertão, G.A., Eschard, R., Mulder, T., Teles, V., Chauveau, B. and **Joseph, P.** (2015) Modelling the deposition of turbidite systems with Cellular Automata numerical simulations: a case study in the Brazilian offshore. Mar. and Petr. Geol. **59**, 166-186.

Allemand, P. and **Brun, J.P.** (1991) Width of continental rifts and rheological layering of the lithosphere. Tectonophysics **188**, 63–69.

Amy, L.A., Kneller, B.C. and **McCaffrey, W.D.** (2007). Facies architecture of the Gres de Peira Cava, SE France: landward stacking patterns in ponded turbiditic basins. J. Geol. Soc. **164**, 143–162.

Athmer, W., Groenenberg, R.M., Luthi, S.M., Donselaar, M.E., Sokoutis, D. and **Willigshofer, E.** (2010) Relay ramps as pathways for turbidity currents: a study combining analogue sandbox experiments and numerical flow simulations. Sedimentology **57**, 806–823.

Badalini, G., Kneller, B. and **Winker, C.D.** (2000) Architecture and processes in the Late Pleistocene Brazos-Trinity turbidite system, Gulf of Mexico Continental slope. In: Deep-water reservoirs of the world (Eds. P. Weimer, R.M. Slatt, J. Coleman, N.C. Rosen, H. Nelson, A.H. Bouma, M.J. Styzen and D.T. Lawrence), Proceedings, 20th Annual Research Conference SEPM, Gulf Coast Section, 304–317.

Beauboeuf, R.T., and **Friedmann, S.J.** (2000) High resolution seismic/sequence stratigraphic framework for the evolution of Pleistocene intraslope basins, western Gulf of Mexico: Depositional models and reservoir analogs. In: Deep-water reservoirs of the world (Eds. P. Weimer, R.M. Slatt, J. Coleman, N.C. Rosen, H. Nelson, A.H. Bouma, M.J. Styzen and D.T. Lawrence), Proceedings, 20th Annual Research Conference SEPM, Gulf Coast Section, 40–60.

Brun, J.P. and **Fort, X.** (2004) Compressional salt tectonics (Angolan margin). Tectonophysics **382**, 129–150.

Brun, J.P. and **Fort, X.** (2011) Salt tectonics at passive margins: geology versus models. Mar. and Petr. Geol. **28**, 1123–1145.

Brunt, R.L., McCaffrey, W.D. and **Kneller, B.** (2004) Experimental modeling of the spatial distribution of grain size developed in a fill-and-spill mini-basin setting. J. Sed. Res. **74**, 438–446.

Cobbold, P.R. and **Szatmari, P. (**1991) Radial gravitational gliding on passive margins. Tectonophysics **188**, 249–289.

Cobbold, P.R., Szatmari, P., Demercian, L.S., Coelho, D. and **Rossello, E.A.** (1995) Seismic and experimental evidence for thin-skinned horizontal shortening by convergent radial gliding on evaporites, deep-water Santos Basin, Brazil. In: Salt tectonics: A global perspective (Eds. M.P.A. Jackson, D.G. Roberts and S. Snelson, S.), AAPG Memoir 65, 305–321.

Colletta, B., Letouzey, J., Pinedo, R., Ballard, J.F. and **Balé, P.** (1991) Computerized X-ray tomography analysis of sandbox models: Examples of thin-skinned thrust systems. Geology **19**, 1063–1067.

Coward, M. and **Stewart, S.** (1995) Salt-influenced structures in the Mesozoic–Tertiary cover of the southern North Sea, U.K. In: Salt tectonics: a global perspective (Eds. M.P.A. Jackson, D.G. Roberts and S. Snelson) AAPG Memoir 65, 229–250.

Demercian, S., Szatmari, P. and **Cobbold, P.R.** (1993) Style and pattern of salt diapirs due to thin-skinned gravitational gliding, Campos and Santos Basins, offshore Brazil. Tectonophysics **228**, 393–433.

Diegel, F.A., Karlo, J.F., Schuster, D.C., Shoup, R.C. and **Tauvers P.R.** (1995) Cenozoic structural evolution and tectonostratigraphic framework of the northern Gulf Coast continental margin. In: Salt tectonics: a global perspective (Eds. M.P.A. Jackson, D.G. Roberts and S. Snelson) AAPG Memoir 65, 109–151.

Duval, B., Cramez, C. and **Jackson, M.P.A.** (1992) Raft tectonics in the Kwanza Basin, Angola. Mar. and Petr. Geol. **9**, 389–404.

Fildani, A., Normark, W.R., Kostic, S. and **Parker, G.** (2006) Channel formation by flow stripping: large-scale scour features along the Monterey East Channel and their relation to sediment waves: Sedimentology **53**, 1265–1287.

Fort, X., Brun, J.P. and **Chauvel, F.** (2004) Salt tectonics on the Angolan margin, synsedimentary deformation processes. AAPG Bull. **88**, 1523–1544.

Gee, M.J.R. and **Gawthorpe, R.L.** (2006) Submarine channels controlled by salt tectonics: examples from 3D seismic data offshore Angola. Marine and Petroleum Geology **23**, 443-458.

Gervais, A., Savoye, B., Mulder, T. and **Gonthier, E.** (2006) Sandy modern turbidite lobes: A new insight from high resolution seismic data. Mar. and Petr. Geol. **23**, 485–502.

Groenenberg, R.M. (2007) Process-based modelling of turbidity-current hydrodynamics and sedimentation. Ph.D. thesis, Delft University of Technology, 200 p.

Groenenberg, R.M., Sloff, C.J. and **Weltje, G.J.** (2009) A high-resolution 2-DH numerical scheme for process-based modelling of 3-D turbidite fan stratigraphy. Computers and Geosciences **35**, 1686–1700.

Groenenberg, R.M., Hodgson, D.M., Prélat, A., Luthi, S.M. and **Flint, S.** (2010) Flow-deposit interactions in submarine lobes: insights from outcrop observations and realizations of a process-based numerical model. J. Sed. Res. **80**, 252–267.

Guerra, M.C.M. and **Underhill, J.R.** (2012) Role of halokinesis in controlling structural styles and sediment dispersal in the Santos basin, offshore Brazil. In: Salt Tectonics, Sediments, Prospectivity (Eds. G.I. Alsop, S.G. Archer, A.J. Hartley, N.T. Grant and R. Hodgkinson), Geol. Soc. London Spec. Publ. 363, 163–206.

Harding, R. and **Husse, M.** (2015) Salt on the move: Multi stage evolution of salt diapirs in the Netherlands North Sea. Mar. and Petr. Geol. **61**, 39-55.

Hodgson, D.M. and **Haughton, P.D.W.** (2004) Impact of syndepositional faulting on gravity current behavior and deep-water stratigraphy: Tabernas-Sorbas Basin, SE Spain. In: Confined Turbidite Systems (Eds. S.A. Lomas and P. Joseph), Geol. Soc. Spec. Publ. 222, 135–158.

Hodgson, D.M., **Flint, S.S., Hodgetts, D., Drinkwater, N.J., Johannessen, E.P.** and **Luthi, S.M.** (2006) Stratigraphic evolution of fine-grained submarine fan systems, Tanqua depocentre, Karoo Basin, South Africa. J. Sed. Res. **76**, 20-40.

Hudec, M.R. and **Jackson, M.P.A.** (2004) Regional restoration across the Kwanza Basin, Angola: Salt tectonics triggered by repeated uplift of a metastable passive margin. AAPG Bull. **88**, 971–990.

Hudec, M.R., Jackson, M.P.A. and **Schultz-Ela, D.D.** (2009) The paradox of minibasin subsidence into salt: clues to the evolution of crustal basins. Geol. Soc. Am. Bull. **121**, 201–221.

Hudec, M.R., Jackson, M.P.A. and **Peel, F.J.** (2013) Influence of deep Louann structure on the evolution of the northern Gulf of Mexico. AAPG Bull. **10**, 1711–1735.

Kneller, B.C. and **McCaffrey, W.D.** (1995) Modelling the effects of salt-induced topography on deposition from turbidity currents. In: Salt, Sediment and Hydrocarbons (Eds. C.S. Travis, H. Harrison, M.R. Hudec, B.C. Vendeville, F.S. Peel and B.E. Perkins), Proceedings, 16th Annual Research Conference SEPM, Gulf Coast Section, 137–145.

Kneller, B.C. and **McCaffrey, W.D.** (1999) Depositional effects of flow non-uniformity and stratification within turbidity currents approaching a bounding slope: deflection, reflection and facies variation. J. Sed. Res. **69**, 980–991.

Kockel, F. (1998) Salt problems in Northwest Germany and the German North Sea sector. In: Geology and Geophysics of Salt Structures (Eds. F. Kockel and R. Marschall, R.). J. Seism. Expl. 7, 219–235.

Kostic, S. (2011) Modeling of submarine cyclic steps: Controls on their formation, migration, and architecture. Geosphere **7**, 294–304.

Kostic, S., and **Parker, G.** (2006) The response of turbidity currents to a canyon–fan transition: Internal hydraulic jumps and depositional signatures. J. Hydr. Res. **44**, 631–653.

Lamb, M.P., Toniolo, H. and **Parker, G.** (2006) Trapping of sustained turbidity currents by intraslope minibasins. Sedimentology **53**, 147–160.

Liro, L.M. and **Coen, R.** (1995) Salt deformation history and postsalt structural trends, offshore southern Gabon, west Africa. In: Salt tectonics: a global perspective (Eds. M.P.A. Jackson, D.G. Roberts and S. Snelson) AAPG Memoir, 65, 323–331.

Loncke, L., Gaullier, V., Mascle, J., Vendeville, B. and **Camera, L.** (2006) The Nile deep-sea fan: an example of interacting sedimentation, salt tectonics, and inherited subsalt paleotopographic features. Mar. and Petr. Geol. **23**, 297–315.

Luthi, S.M. (1981) Experiments on non-channelized turbidity currents and their deposits. Marine Geology **40**, M59–M68.

Marton, L.G., Tari, G.C. and **Lehmann, C.T.** (2000) Evolution of the Angolan passive margin, West Africa, with emphasis on post-salt structural styles. In: Atlantic rifts and continental margins (Eds. W.U. Mohriak and M. Talwani). AGU Geophysical Monograph 115, 129–149.

McCaffrey, W.D. and **Kneller, B.C.** (2001) Process controls on the development of trap potential on the margins of confined turbidite systems and aid to reservoir evaluation. AAPG Bull. **85**, 971–988.

McClay, K.R. (1990) Extensional fault systems in sedimentary basins: a review of analogue model studies. Mar. and Petr. Geol. **7**, 206–233.

Mohriak, W.U., Azatmari, P. and **Anjos, S.** (2012) Salt: geology and tectonics of selected Brazilian basins in their global context. In: Salt Tectonics, Sediments, Prospectivity (Eds. G.I. Alsop, S.G. Archer, A.J. Hartley, N.T. Grant and R. Hodgkinson), Geol. Soc. London Spec. Publ. 363, 131–158.

Moody, J.D., Pyles, D.R., Clark, J. and **Bouroullec, R.** (2012) Quantitative outcrop characterization of an analog to weakly confined submarine channel systems: Morillo 1 Member, Ainsa Basin, Spain. AAPG Bull. **96**, 1813–1841.

Oluboyo, A.P., Gawthorpe, R.L., Bakke, K. and **Hadler-Jacobsen, F.** (2014) Salt tectonic control on deep-water turbidite depositional systems: Miocene, southwestern Lower Congo Basin, offshore Angola. Basin Res. **26**, 597–620.

Parker, G., Fukushima, Y. and **Pantin, H.M**. (1986) Self-accelerating turbidity currents. J. Fluid. Mech. **171**, 145–181.

Prather, B.E., Booth, J.R., Steffens, G.S. and **Craig**, **P.A.** (1998) Classification, lithologic calibration, and stratigraphic succession of seismic facies of intraslope basins, deep-water Gulf of Mexico. AAPG Bull**. 82**, 701–728.

Prather, B.E. (2000) Calibration and visualization of depositional process models for above-grade slopes: A case study from the Gulf of Mexico. Mar. and Petr. Geol. **17**, 619–638.

Prather, B.E., Pirmez, C. and **Winker, C.D.** (2012) Stratigraphy of linked intraslope basins: Brazos-Trinity system western Gulf of Mexico. SEPM Spec.Publ. **99**, 83–109.

Roberts, M.J., Metzgar, C.R., Liu, J. and **Lim, S.J.** (2004) Regional assessment of salt weld timing, Campos Basin, Brazil. In: Salt-sediment interactions and hydrocarbon prospectivity: Concepts, applications, and case studies for the 21st Century (Eds. P.J. Post, D.L. Olson, K.T. Lyons, S.L Palmes, P.F. Harrison and N.C. Rosen), Proceedings, 24th Annual Research Conference SEPM, Gulf Coast Section, 371–389.

Rowan, M.G. and **Weimer, P.** (1998) Salt-sediment interaction, central Louisiana outer shelf and upper slope, northern Gulf of Mexico. AAPG Bull. **82**, 1055–1082.

Satur, N., Hurst, A., Cronin, B.T., Kelling, G. and **Gürbüz, K**. (2000) Sand body geometry in a sand-rich, deep-water clastic system, Miocene Cingöz Formation of southern Turkey. Mar. and Petr. Geol. **17,** 239–252.

Shanmugam, G. and **Moiola, R.J.** (1991) Types of submarine fan lobes: models and implications. AAPG Bull. **75**, 156–179.

Shanmugam, G. (2000) 50 years of the turbidite paradigm (1950s–1990s): deep-water processes and facies models. Mar. and Petr. Geol **17**, 85–342.

Sinclair H.D. and **Tomasso, M.** (2002) Depositional evolution of confined turbidite basins. J. Sed. Res. **72**, 451–456.

Smith, R. (2004) Silled sub-basins to connected tortuous corridors: sediment distribution systems on topographically complex sub-aqueous slopes. In: Confined Turbidite Systems (Eds. S.A. Lomas and P. Joseph), Geol. Soc. Spec. Publ. 222, 23–44.

Sokoutis, D. and **Willingshofer, E.** (2011) Decoupling during continental collision and intraplate deformation. Earth and Planet. Sci. Let. **305**, 435-444.

Spychala, Y.T., Hodgson, D.M., Flint, S.S. and **Mountney, N.** (2015) Constraining the sedimentology and stratigraphy of submarine intraslope lobe deposits using exhumed examples from the Karoo Basin, South Africa. Sedimentary Geology, **322**, 67-81.

Talling, P.J.; Allin, J.; Armitage, D.A.; Arnott, R.W.C.; Cartigny, M.J.B.; Clare, M.A.; Felletti, F.; Covault, J. A.; Girardclos, S.; Hansen, E.; Hill, P.R.; Hiscott, R.N.; Hogg, A.J.; Clarke, J.H.; Jobe, Z.R.; Malgesini, G.; Mozzato, A.; Naruse, H.; Parkinson, S.; Peel, F.J.; Piper, D.J.W.; Pope, E.; Postma, G.; Rowley, P.; Sguazzini, A.; Stevenson, C.J.; Sumner, E.J.; Sylvester, Z.; Watts, C. and **Xu, J. (**2015) Key future directions for research on turbidity currents and their deposits. J. Sed. Res. **85.** 153-169.

Van Andel, T.H. and **Komar, D.** (1969) Ponded sediments of the Mid-Atlantic Ridge between 22° and 23° North Latitude. Geol. Soc. Am. Bull. **80**, 1163–1190.

Vendeville, B.C. and **Cobbold, P.R. (**1988) How normal faulting and sedimentation interact to produce listric fault profiles and stratigraphic wedges. J. of Struct. Geol. **10**, 649–659.

Vendeville, B.C. and **Jackson, M.P.A.** (1992a). The rise of diapirs during thin-skinned extension. Mar. and Petr. Geol. **9**, 331–353.

Vendeville, B.C. and **Jackson, M.P.A.** (1992b) The fall of diapirs during thin-skinned extension. Mar. and Petr. Geol. **9**, 354–371.

Wang, X. (2015) Turbidite flows and their deposits on slopes with minibasins. Ph.D. thesis, Delft University of Technology, 184 p.

Weijermars, R. (1986a) Finite strain of laminar flows can be visualized in SGM36-polymer. Naturwissenschaften **73**, 33–34.

Weijermars, R. (1986b) Flow behaviour and physical chemistry of bouncing putties and related polymers in view of tectonic laboratory applications. Tectonophysics **124**, 325–358.

Weijermars, R., Jackson, M.P.A. and **Vendeville, B.** (1993) Rheological and tectonic modeling of salt provinces. Tectonophysics **217**, 143–174.

Weimer, P., Varnai, P., Budhijanto, F.M., Acosta, Z. M., Martinez, R.E., Navarro, A.F., Rowan, M.G., McBride, B.C., Villamil, T., Arango, C., Crews, J.R. and **Pulham, A.J.** (1998) Sequence stratigraphy of Pliocene and Pleistocene turbidite systems, northern Green Canyon and Ewing Bank (offshore Louisiana), northern Gulf of Mexico. AAPG Bull. **82**, 918–960.

Willingshofer, E., Sokoutis, D. and **Burg, J.-P.** (2005) Lithospheric-scale analogue modeling of collision zones with a pre-existing weak zone. Geol. Soc. Spec. Publ. 243, 277-294.

Willingshofer, E., Sokoutis, D., Luth, S.W., Beekman, F. and **Cloetingh, S.** (2013) Subduction and deformation of the continental lithosphere in response to plate and crust-mantle coupling. Geology **41**, 1239-1242.

Winker, C.D. (1996) High-resolution seismic stratigraphy of a Late Pleistocene submarine fan ponded by salt-withdrawal mini-basins on the Gulf of Mexico continental slope. Proceedings, Offshore Technology Conference, 619–628.

Xu, J.P., Noble, M.A. and **Rosenfeld, L.K.** (2004) In-situ measurements of velocity structure within turbidity currents. Geophys. Res. Let. 31 (9).

Zeng, J., Lowe, D. R., Prior, D. B., Wisenam, W. J., Jr, and **Bornhold, B. D.** (1991) Flow properties of turbidity currents in Bute inlet, British Columbia. Sedimentology **38**, 975–996.

Zhong, G., Cartigny, M.J.B., Kuang, Z. and **Wang, L.** (2015) Cyclic steps along the South Taiwan Shoal and West Penghu submarine canyons on the northeastern continental slop of the South China Sea. Bull. Geol. Soc. Am. **127**, 804-824.

FIGURE CAPTIONS

Fig. 1. Setup of the sand-silicone experiment. A: Oblique top views showing the model set-up, the dimensions and the boundary confinements. B: Longitudinal cross-section of the model showing the internal layering. Plate 1 is tilted at an angle $\alpha = 4°$ to initiate the experiment.

Fig. 2. A: An artificial illumination of the sand-silicone experiment after 68 hours. Structural elements are indicated as follows: D = Diapir; Fd = Fold; T = Thrust; MB = Minibasin. B: Longitudinal cross-section, with the three main structural domains and the location of the minibasins indicated.

Fig. 3. A: 3D view of the topographic area used in this study as the seabed bathymetry analogue. The main geomorphological elements include (a) a leveed channel, (b) a well-confined minibasin, (c) diapiric ridges and (d) two poorly-confined minibasins. The blue arrow indicates the inflow point and the initial direction of the simulated turbidity currents. The vertical exaggeration is 20x. B: Plan view contour map of the same area with red hues indicating the slope angles as the steepest descent or ascent at any grid node on the surface. Blue arrow indicates upslope entry point.

Fig. 4. Flow evolution of events 1, 25 and 45, representative for the initial ponding stage, the fill-and-spill stage, and the retrogradational ponding stage. Shown are the flow thicknesses, the velocity vectors and the densimetric Froude number (only as being super- or subcritical). The time slices were chosen to illustrate the main phases of these

three flows and are therefore not equal for the three experiments. Note that flow event 25 lasted 2.5 hours until the last sediment had settled; the ponding flows were in general shorter lived. In event 45 the hydraulic jumps in the channel can be seen.

Fig. 5. Maps showing the bed thicknesses and mean grain sizes (grouped into four categories) for the beds resulting from flow events 1, 2, 20, 30, 40, 60, 80 and 100. The extended depositional area is well seen in beds 2, 20 and 30, with some coarse sediment reaching the lower minibasins but also forming levees. Areas of net erosion, shown in blue on the bed thickness maps, occur in the channel and the leeside of the confining ridge. Bed 40 already shows the retrogradational development, which continues in beds 60, 80 and 100 where the cyclic steps are clearly seen.

Fig. 6. Maps showing the depositional thicknesses of the beds formed in the fill-and-spill-dominated phase (events 2-40), the ponding-dominated stage (events 41-100) and the total depositional thickness of all 100 events. Note that the thickness colour scale bar changes in each map.

Fig. 7. Artificially illuminated maps showing the bathymetries after events 40 (A), 70 (B) and 100 (C). Notice that there are no changes downstream of the upper minibasin as these snapshots are all from the retrogradational ponding stage. D: The bathymetric evolution of the upper minibasin in a longitudinal cross-section along the line indicated in C, in steps of 10 flow events. Round dots indicate potential “spill points” of the upper minibasin while black squares indicate the location of the lowest points in the sections.

This cross-section illustrates that the latter differ substantially from the depocentres. E: The average counterslope gradient, defined here as the angle from the lowest point to the “spill-over point”. It shows a decrease during the fill-and-spill-dominated phase then a jump to a much higher gradient as a basin-internal ridge becomes the new spill-point, and from there throughout the ponding-dominated phase again a monotonic decrease of the gradient.

Fig. 8. A: The spatial division of the bathymetry into five depositional domains. The leeward side of the confining ridge contains only very minor deposits and is not considered here. B: Proportion of the sediment volumes in the five domains for the seven depositional units, with U1 belonging to the initial ponding stage, U2-U4 to the fill-and-spill stage, U5 to the transitional stage, and U6-U7 to the retrogradational ponding stage. Notice the relatively constant sediment distribution in the fill-and-spill stage and the continuous backstepping thereafter.

Fig. 9. Longitudinal (A-A') cross-section along the main flow axis shown in the insert, with the colours indicating the tops of the seven depositional units and the dots their respective depocentres. Notice the general upstream migration, for the last unit even in a punctuated jump. This longitudinal compensation contrasts with the lateral compensation exhibited in all three minibasins, as shown in the across-flow cross-section for the upper minibasin (B-B'), the first lower minibasin (C-C') and the second lower minibasin (D-D').

Fig. 10. Stratigraphic evolution of basins II and IV in the Brazos-Trinity depositional system (modified from Prather et al., 2012), with the colours representing the different interpreted depositional series. Black dots indicate the interpreted depocentres of each series. After the first two units shown in pink and dark blue the two minibasins had reached approximately their present shape, so salt tectonics are considered a minor influence in the backstepping of the depocentres.

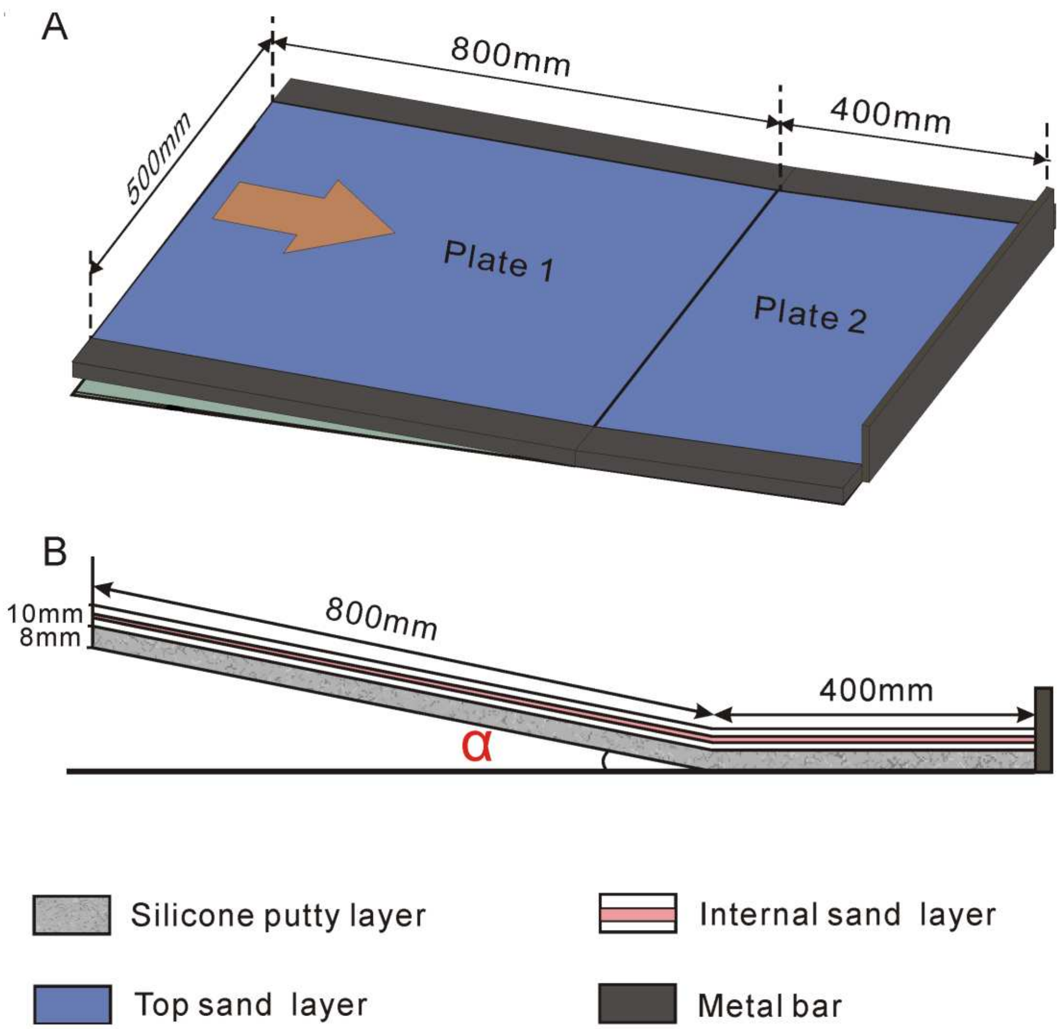

Figure 1

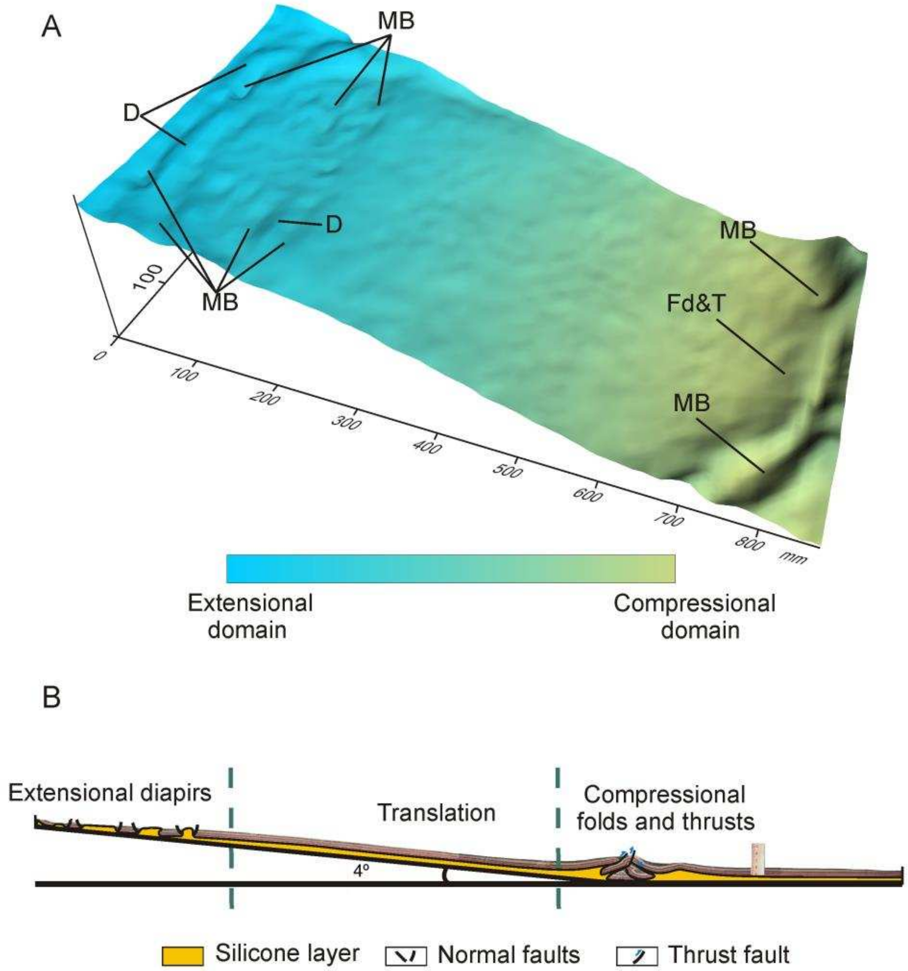

Figure 2

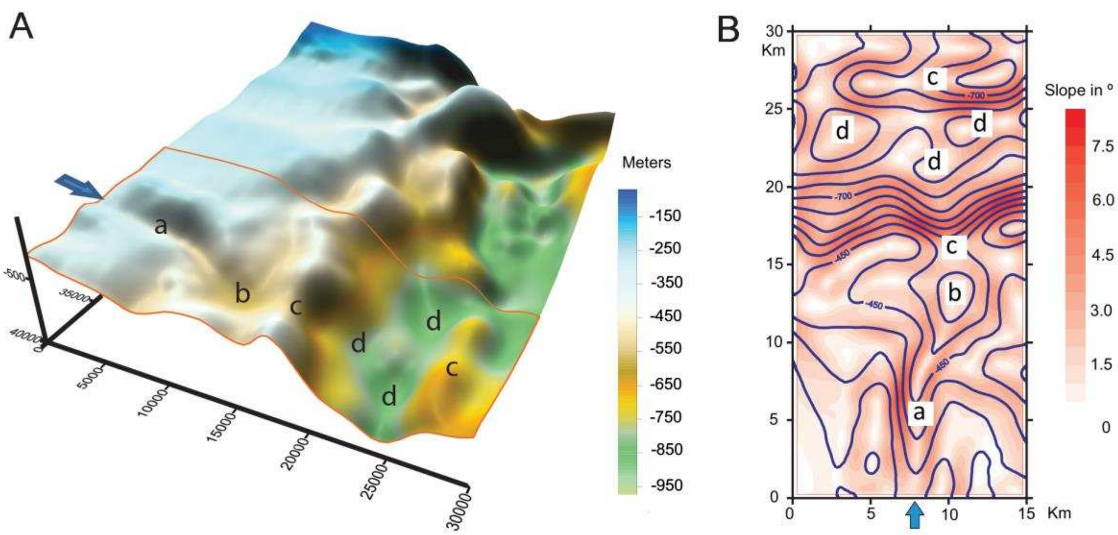

Figure 3

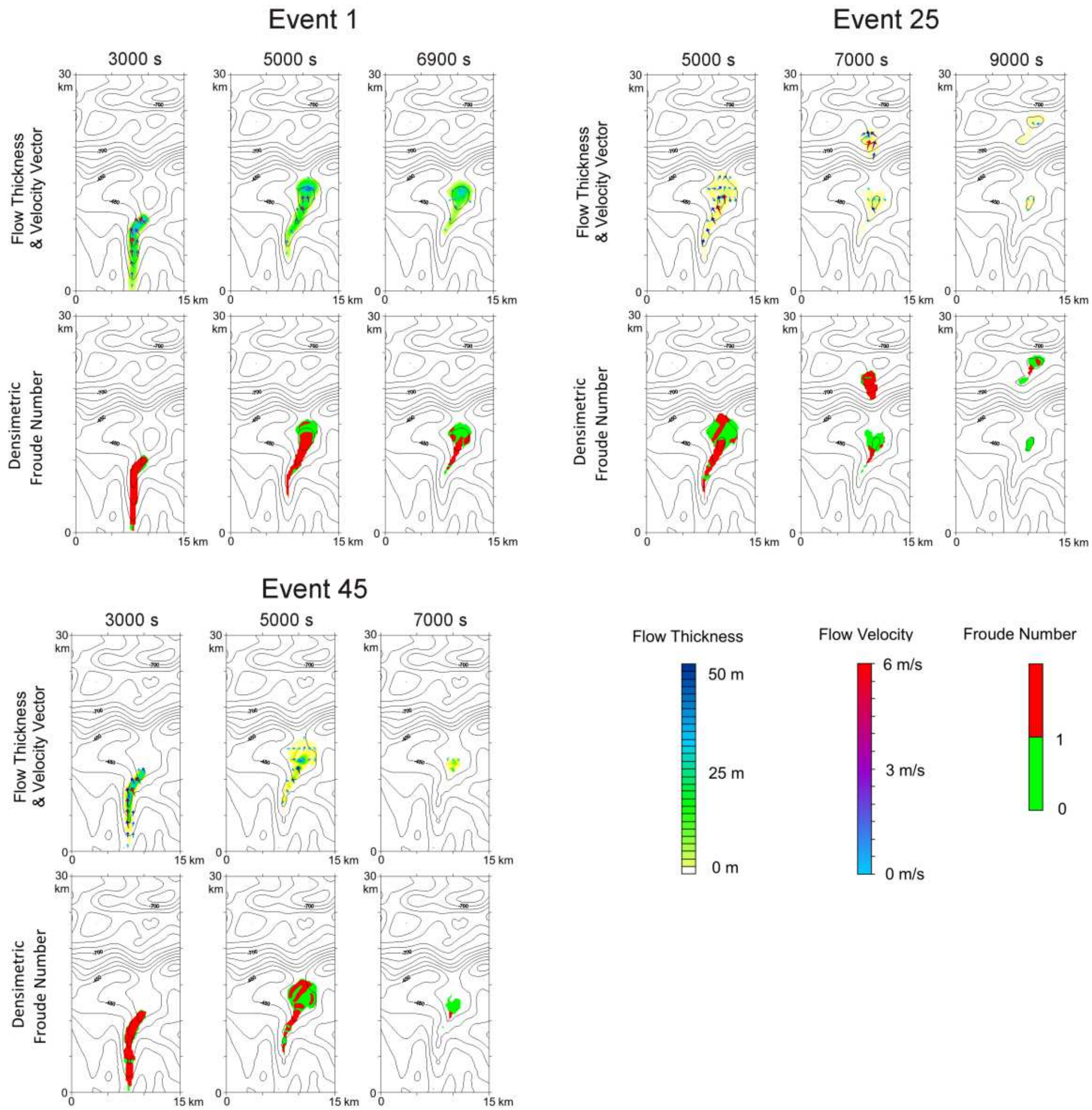
Event 1
3000 s
5000 s
6900 s
Event 25
5000 s
7000 s
9000 s
Event 45
3000 s
5000 s
7000 s
Flow Thickness & Velocity Vector
Densimetric Froude Number
30 km
0
15 km
Flow Thickness
50 m
25 m
0 m
Flow Velocity
6 m/s
3 m/s
0 m/s
Froude Number
1
0

Figure 4

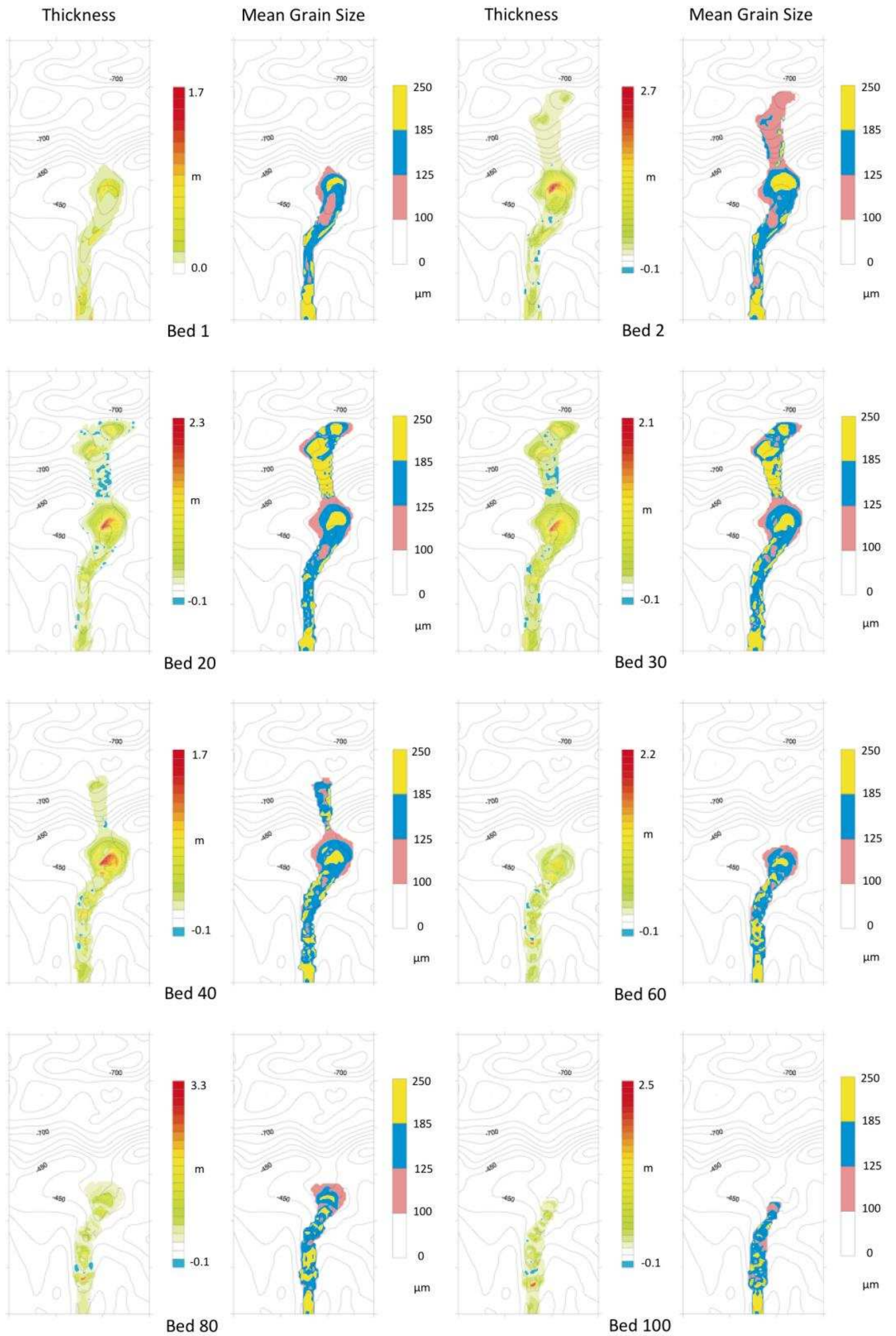
Thickness
Mean Grain Size
Thickness
Mean Grain Size
1.7
m
0.0
250
185
125
100
0
µm
Bed 1
2.7
m
-0.1
250
185
125
100
0
µm
Bed 2
2.3
m
-0.1
250
185
125
100
0
µm
Bed 20
2.1
m
-0.1
250
185
125
100
0
µm
Bed 30
1.7
m
-0.1
250
185
125
100
0
µm
Bed 40
2.2
m
-0.1
250
185
125
100
0
µm
Bed 60
3.3
m
-0.1
250
185
125
100
0
µm
Bed 80
2.5
m
-0.1
250
185
125
100
0
µm
Bed 100

Figure 5

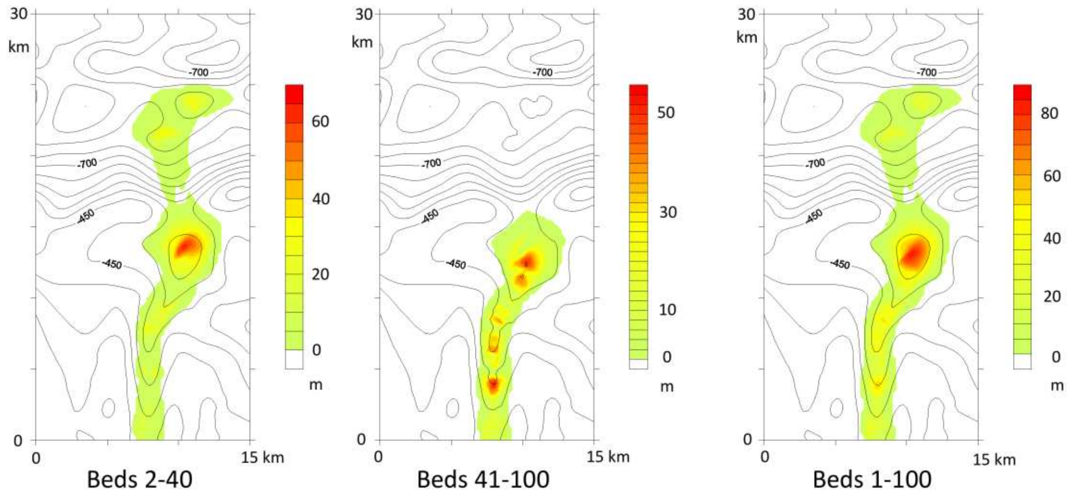

Figure 6

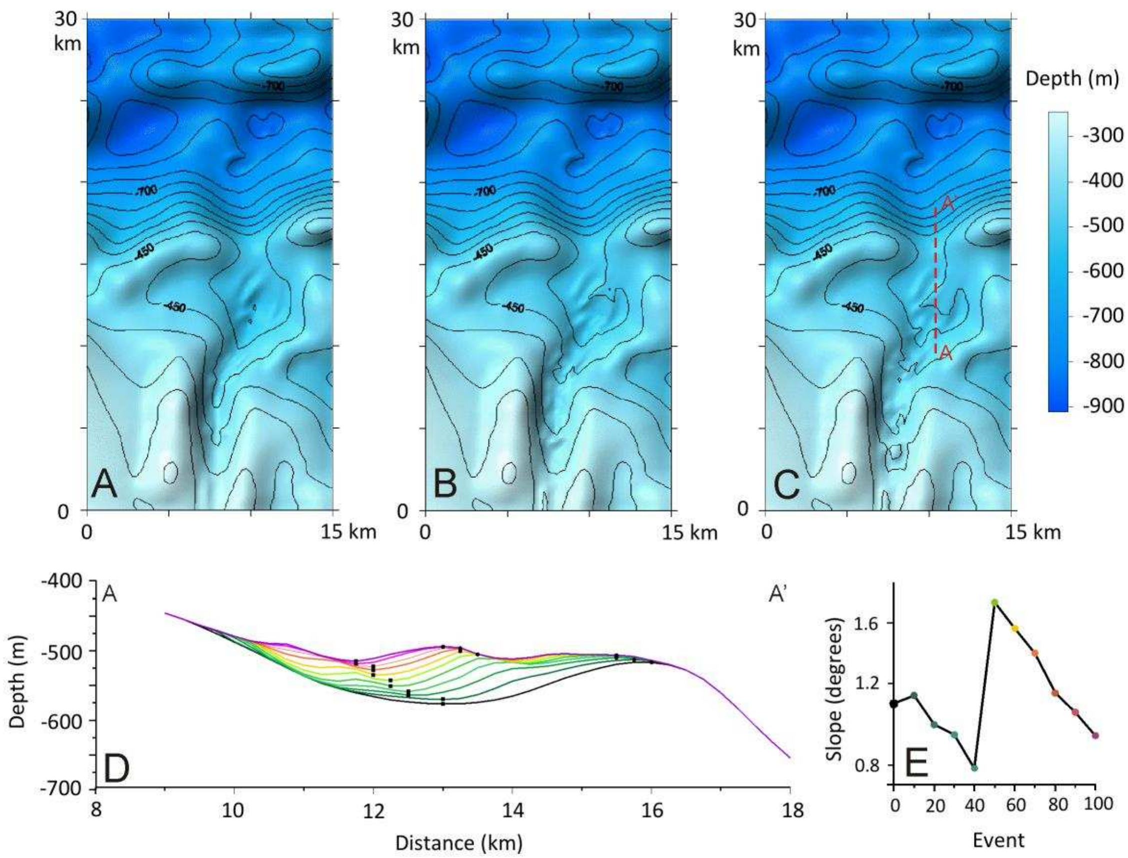

Figure 7

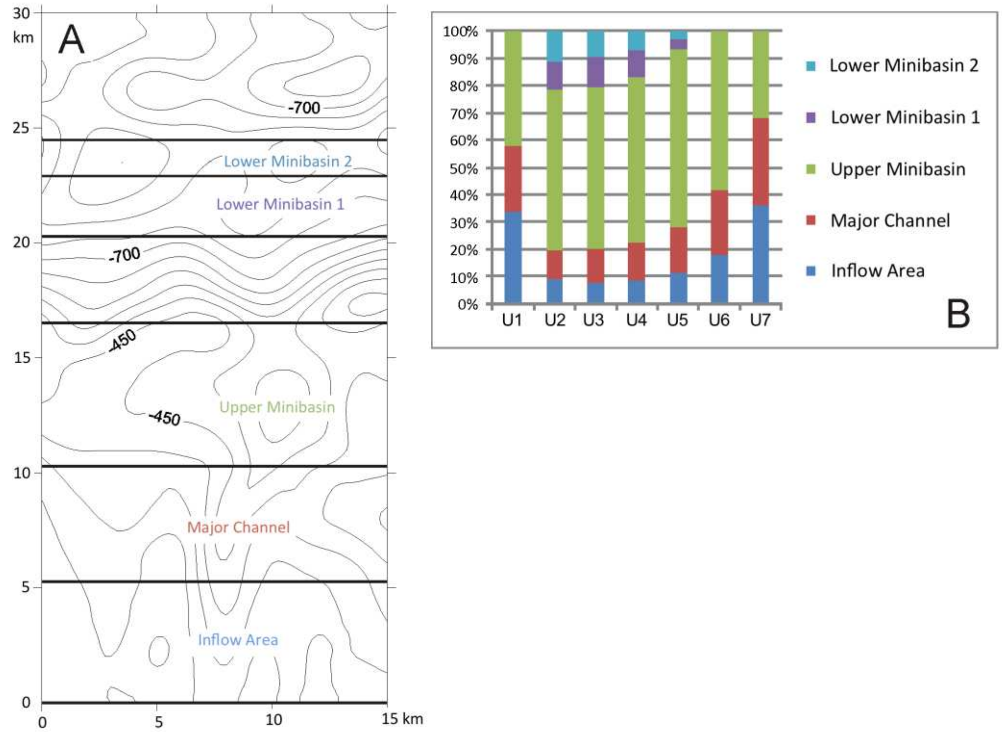

Figure 8

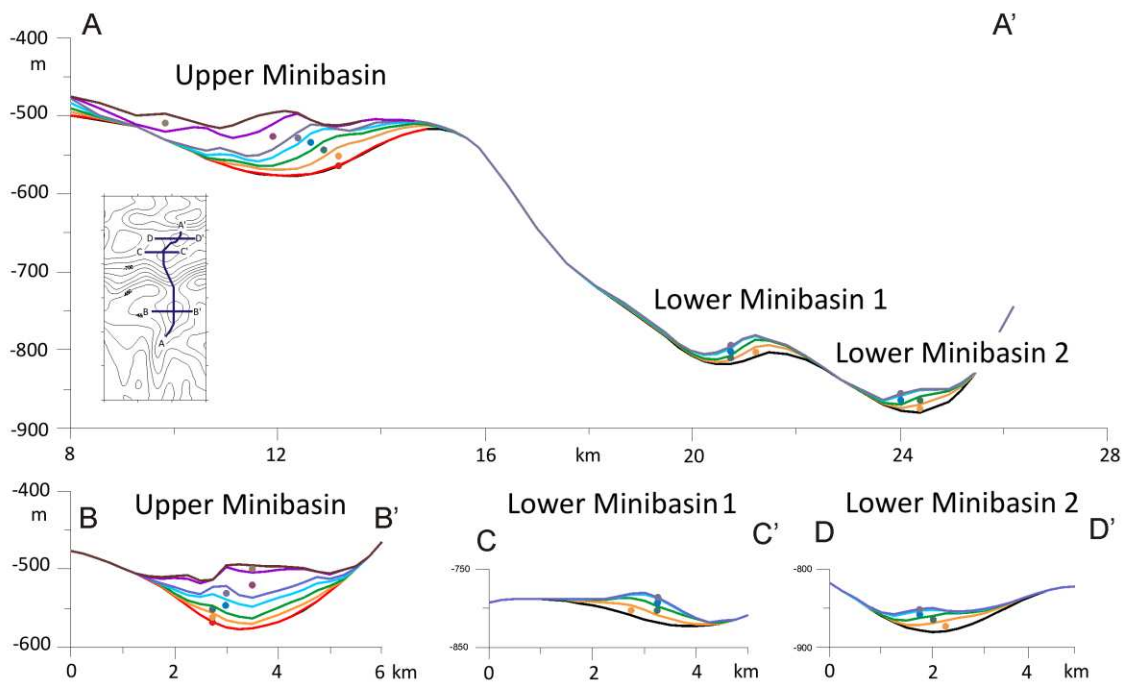

Figure 9

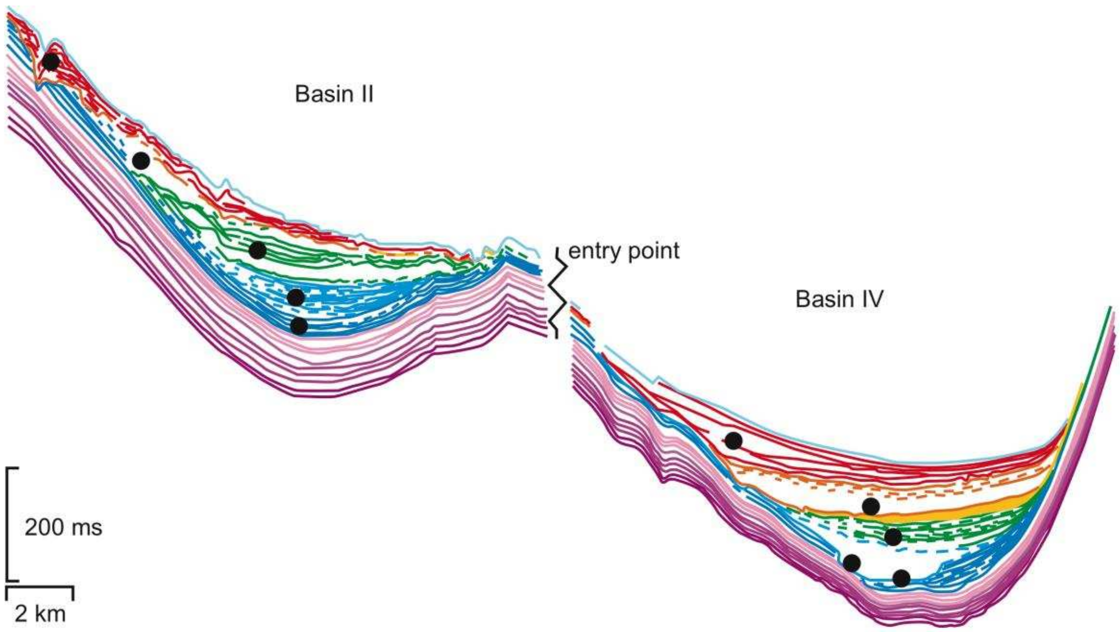

Figure 10

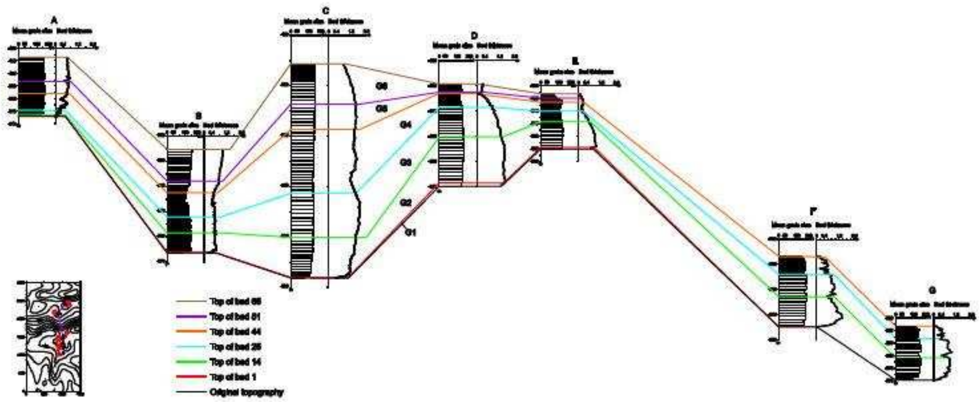

Figure 5.12: Cross-section showing the longitudinal isochronous correlation of the stratigraphy (supercritical non-equilibrium inflows) in the three minibasins. Seven spots are selected to display the mean grain-size column and layer thickness profile. Spots A, B, C and D are along the central longitudinal axis of the upper well-confined nimibasin, spot F is located at the thickest deposit of the first lower minibasin, and spot G is in the second lower minibasin (see the map showing these locations). Six stratigraphic groups are recognized (G1, G2, G3, G4, G5 and G6). For detailed explanations see text.

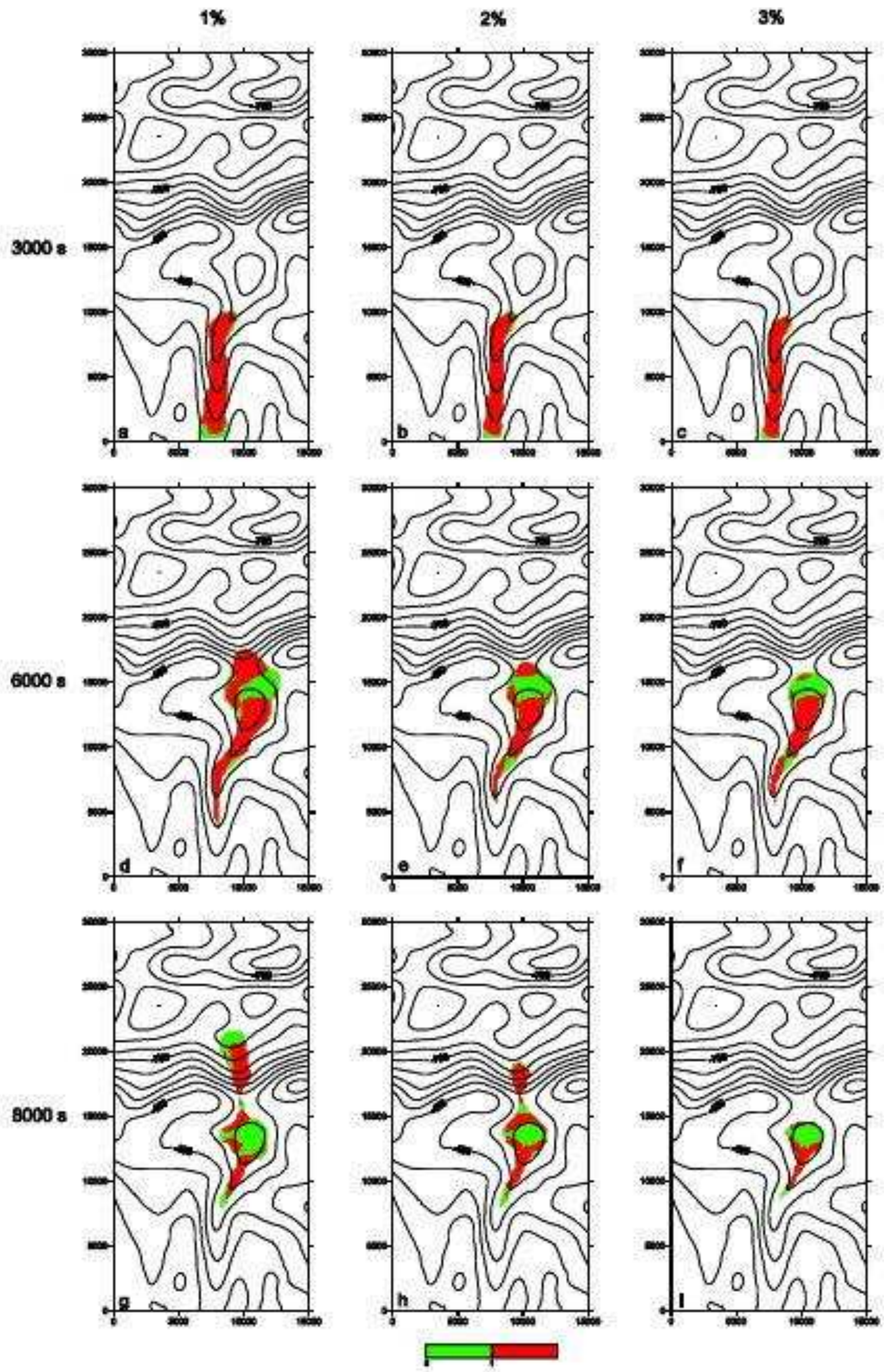

Figure 5.30: Densiometric Froude number evolution of event 2 (at 3000s, 6000s and 8000s) of the first group of subcritical equilibrium inflows (1%, 2% and 3%). All maps are superposed onto the elevation contour map of the original topography.